IOP Publishing Plasma Sources Science and Technology
Plasma Sources Sci. Technol. **32** (2023) 115003 (11pp) https://doi.org/10.1088/1361-6595/ad0432

Experimental validation of particle-in-cell/Monte Carlo collisions simulations in low-pressure neon capacitively coupled plasmas

Chan-Won Park[1,2,8], B Horváth[3,4,8], A Derzsi[3], J Schulze[5], J H Kim[1], Z Donkó[3] and Hyo-Chang Lee[6,7,*]

[1] Korea Research Institute of Standards and Science, Daejeon 34113, Republic of Korea
[2] Department of Physics, Chungnam National University, Daejeon 34134, Republic of Korea
[3] Institute for Solid State Physics and Optics, Wigner Research Centre for Physics, 1121 Budapest, Hungary
[4] ELTE Eötvös Loránd University, Budapest, Hungary
[5] Chair of Applied Electrodynamics and Plasma Technology, Faculty of Electrical Engineering and Information Sciences, Ruhr University Bochum, 44801 Bochum, Germany
[6] School of Electronics and Information Engineering, Korea Aerospace University, Goyang, Gyeonggi-do 10540, Republic of Korea
[7] Department of Semiconductor Science, Engineering and Technology, Korea Aerospace University, Goyang 10540, Republic of Korea

E-mail: plasma@kau.ac.kr

Received 18 July 2023, revised 6 October 2023
Accepted for publication 17 October 2023
Published 2 November 2023

Abstract

Plasma simulations are powerful tools for understanding fundamental plasma science phenomena and for process optimisation in applications. To ensure their quantitative accuracy, they must be validated against experiments. In this work, such an experimental validation is performed for a one dimensional in space and three dimensional in velocity space particle-in-cell simulation complemented with the Monte Carlo treatment of collision processes of a capacitively coupled radio frequency plasma driven at 13.56 MHz and operated in neon gas. In a geometrically symmetric reactor the electron density in the discharge centre and the spatio-temporal distribution of the electron impact excitation rate from the ground into the Ne $2p_1$ level are measured by a microwave cutoff probe and phase resolved optical emission spectroscopy, respectively. The measurements are conducted for electrode gaps between 50 mm and 90 mm, neutral gas pressures between 20 mTorr and 50 mTorr, and peak-to-peak values of the driving voltage waveform between 250 V and 650 V. Simulations are performed under identical discharge conditions. In the simulations, various combinations of surface coefficients characterising the interactions of electrons and heavy particles with the anodised aluminium electrode surfaces are adopted. We find, that the simulations using a constant effective heavy particle induced secondary electron (SE) emission coefficient of 0.3 and a realistic electron–surface interaction model (which considers energy-dependent and material specific elastic and inelastic electron reflection, as well as the emission of true SEs from the surface) yield results which are in good quantitative agreement with the experimental data.

[8] First author with equal contribution.
[*] Author to whom any correspondence should be addressed.

Keywords: capacitively coupled plasma, particle-in-cell/Monte Carlo collisions simulation, phase resolved optical emission spectroscopy, secondary electron emission, plasma–surface interaction, plasma diagnostics

1. Introduction

Low-pressure capacitively coupled plasmas (CCPs) have a wide range of applications such as etching and deposition processes for semiconductor and display device fabrication [1–4]. To optimise and control such plasma processes, fundamental insights into the plasma physics and chemistry are required to understand the effects of external control parameters such as the driving voltage/power, the reactor geometry and the gas mixture on process relevant discharge properties [5].

A variety of experimental and computational studies focused on different aspects of CCP operation has been conducted in the past. These include computational investigations based on fully kinetic particle-in-cell simulations complemented with the Monte Carlo treatment of collision processes (PIC/MCC) [6–19] as well as hybrid fluid/kinetic simulations [19–21] and experimental studies based on different plasma diagnostics.

For instance, PIC/MCC simulations, that are one dimensional (1D) in space and three dimensional in velocity space (1d3v), were used to study the basic mechanisms of the formation of ion energy distribution functions (IEDFs) at the electrodes of single- and dual-frequency CCPs operated in reactive gas mixtures [22]. Limitations of the separate control of the ion flux and the mean ion energy at the electrodes in dual-frequency CCPs operated at strongly different frequencies were revealed based on such simulations as well, explained by the effects of frequency coupling and secondary electrons (SEs) [23, 24]. Both by means of experiments and simulations, voltage waveform tailoring was demonstrated to overcome such limitations and provide an improved separate control of the mean ion energy and flux [23, 25–28] as well as control over the IEDF shape [29–32].

Hybrid simulations were used to study the effects of external control parameters on the plasma chemistry in reactive CCPs, e.g. the generation of reactive radicals [33, 34]. In separate experimental studies and for different discharge conditions, laser induced fluorescence [35–37] and mass spectrometry [38, 39] were used to measure radical concentrations.

The spatio-temporal dynamics of the electron power absorption was studied both computationally and experimentally as the fundament of knowledge based plasma process development and control. Electropositive CCPs operated at low pressures and voltages were found to operate in the α-mode [40–42], where ambipolar electron power absorption during the sheath expansion phase leads to the generation of energetic electron beams that propagate into the plasma bulk [43]. At higher pressures/voltages or in case of the presence of an electrode with a high SE yield, such discharges were found to operate in the γ-mode, where ionisation by SE avalanches inside the radio frequency (RF) sheaths due to ion-induced SE emission (SEE) from the electrodes dominates [23, 40, 44]. Electronegative and/or high pressure CCPs often operate in the drift–ambipolar mode, where strong drift and ambipolar electric fields in the plasma bulk accelerate electrons to high energies [45–48]. At low driving frequencies, electronegative discharges can also operate in the striation mode as a consequence of the interaction of positive and negative ions with the RF electric field in the plasma bulk [49, 50].

Such fundamental investigations have led to the development of distinct methods of controlling the electron energy distribution function such as accelerating electrons in a controlled way to penetrate deeply into high aspect ratio dielectric etch profiles to compensate positive surface charges inside such trenches that would otherwise cause profile distortion and etch stops [31, 51–53]. Multi-dimensional simulations have been used to study radial plasma non-uniformities and develop concepts for their prevention/compensation such as structured, graded conductivity and segmented electrodes [54–57]. Some of these concepts have been verified qualitatively based on experiments performed under different discharge conditions [58, 59].

These fundamental insights and control concepts were typically developed based on qualitatively correct simulation results, that can predict parameter trends correctly. Code-to-code benchmarks were performed in some cases to ensure identical computational results of several codes under identical discharge conditions [60, 61]. While these previous works are important and of high value, simulation based plasma process development requires quantitatively accurate results in many cases. To ensure such quantitative accuracy, simulation results must be validated against experiments to make sure that they yield correct absolute values of plasma parameters such as the electron and radical densities. Code-to-code benchmark studies are not sufficient for that purpose, since they do not ensure realistic simulation results that agree with experiments. Experimental validation studies of plasma simulations are challenging, since they must be performed separately for different gas mixtures, reactor geometries, and discharge conditions. Moreover, well defined experimental systems must be used to ensure that their settings (reactor geometry, wall materials, etc) agree with those assumed in the simulation. For instance, geometrically symmetric CCP reactors must be used for validating 1d3v PIC/MCC simulations, which inherently assume such reactor symmetry. Ideally, multiple plasma parameters should be measured experimentally as a function of the external control parameters and compared to the computational results. This requires using multiple diagnostics in the experiment.

Due to these challenges such systematic experimental validation studies are rare, but represent an important topic of current research in low temperature plasma science. Such a multi-diagnostic experimental validation was recently performed for low pressure single frequency CCPs operated in argon gas in a geometrically symmetric reactor [62]. The plasma density, the gas temperature, the IEDF, and the spatio-temporal distribution of the excitation rate of the Ar $2p_1$ level were measured as functions of the neutral gas pressure and the driving voltage amplitude. Good quantitative agreement with results obtained from 1d3v PIC/MCC simulations was found for a distinct set of surface coefficients used in the simulation for ion-induced SEE and effective electron reflection at the stainless steel electrodes. In a separate study, a computationally assisted diagnostics was developed to determine the ion-induced SE emission coefficient (SEEC) and the electron reflection probability for various electrode materials [63]. The basis of comparison is the IEDF obtained from measurement and PIC/MCC simulations assuming different sets of surface coefficients (which are input parameters of such simulations). This technique is conceptually similar to γ-CAST, the computationally assisted spectroscopic technique proposed in [64] for the determination of the ion-induced SEEC of electrodes exposed to CCPs based on their effects on the spatio-temporal electron impact excitation dynamics. In different mixtures of neon and oxygen gas, the spatio-temporal distributions of the Ne $2p_1$ excitation rate measured by phase resolved optical emission spectroscopy (PROES) were compared successfully to results of 1d3v PIC/MCC simulations at different neutral gas pressures and gas mixing ratios [65]. Again, a strong sensitivity of the simulation results on these surface coefficients was observed and good agreement with experimental measurements was only found for distinct choices of these input parameters.

These experimental validation studies and additional computational investigations [7, 12, 44, 66–72] show that the discharge characteristics may significantly be influenced by plasma–surface interactions. Therefore, a careful selection of the most important surface processes to be included in simulations and a realistic implementation of these is important for the accuracy of the computational results. In inert gases and at low pressures of a few Pa the most important processes are electron emission and reflection due to ion– and electron–surface interactions. SEE due to excited neutrals and photons [73] as well as fast neutrals [74] can play a moderate role, too. The efficiency of SEE and electron reflection processes depends on the energy and the angle of incidence of the incoming particle as well as on the surface material [70, 71, 75, 76]. The ion-induced SEE process is characterised by the corresponding SEEC, γ. At low ion impact energies the ion-induced SEE is determined by the Auger effect and models exist to calculate the corresponding SEEC for metal surfaces [44, 77]. At higher ion energies kinetic knockout effects lead to an increase of the ion-induced SEEC as a function of the ion energy [75, 78]. In the case of electron impact, various processes, including elastic and inelastic reflection and the emission of true SEs, contribute to the electron flux that leaves the surface. These processes are characterised by the coefficients η_e, η_i, and δ, respectively. Electron-induced SEs can impact plasma parameters such as the plasma density, the electronegativity, the metastable density in case of reactive gases and the ionisation dynamics [70, 71, 79–81].

SEs induced by ions (γ-electrons) gain energy from the electric field within the sheaths and contribute to the ionisation/excitation dynamics. Therefore, the γ-electrons may even change the dominant discharge operation mode of a CCP from the α- to the γ-mode [12, 40]. In CCPs operated with SiO_2 electrodes at low pressures and high voltage amplitudes, energetic ion-induced SEs generated and accelerated towards the plasma bulk at one electrode can reach the opposite electrode during the local sheath collapse and cause the emission of electron induced SEs (true SEs, δ-electrons) [70]. Such δ-electrons can also be generated by energetic δ-electrons created earlier or by bulk electrons (which are electrons generated via ionisation process) that reach the electrode during sheath collapse. Depending on the time of generation, δ-electrons can be accelerated towards the bulk by the residual sheath potential or by the expanding sheath. As the electron-induced SEEC can be much higher than the heavy particle induced SEECs [70, 71, 79, 80], δ-electrons can contribute strongly to the ionisation and their presence can significantly enhance the plasma density.

The aim of this study is to validate the PIC/MCC simulation model and code for Ne gas, by conducting a systematic comparison of experimental and computational results for (i) the electron density and (ii) the spatio-temporally resolved electron impact excitation rate of the Ne $2p_1$ level under various plasma conditions. CCPs operated in neon are important for the spectroscopy of RF discharges, since the Ne $2p_1$ excited level has beneficial properties for nanosecond time resolved spectroscopy [82, 83]. Neon gas can be used as a non-invasive tracer gas at low concentrations due to its high ionisation threshold energy and, thus, allows analysing the spatio-temporally resolved dynamics of energetic electrons by revealing the space and time resolved electron impact excitation rate from the ground into the Ne $2p_1$ level [41, 65, 84].

The paper is structured in the following way. In section 2, the experimental setup of the CCP with the diagnostic systems for the microwave cutoff probe measurements and for PROES measurements are introduced. In section 3, some details of the PIC/MCC simulations are presented. Section 4 includes the comparison of the experimental and computational results. Finally, conclusions are drawn in section 5.

2. Experimental setup

Figure 1 shows a schematic diagram of the CCP reactor including the plasma diagnostics used in this work, i.e. the instrumentation for the microwave cutoff probe measurements and the PROES system. In order to realise a symmetric plasma configuration for meaningful comparisons of experimental and computational results of 1d3v PIC/MCC

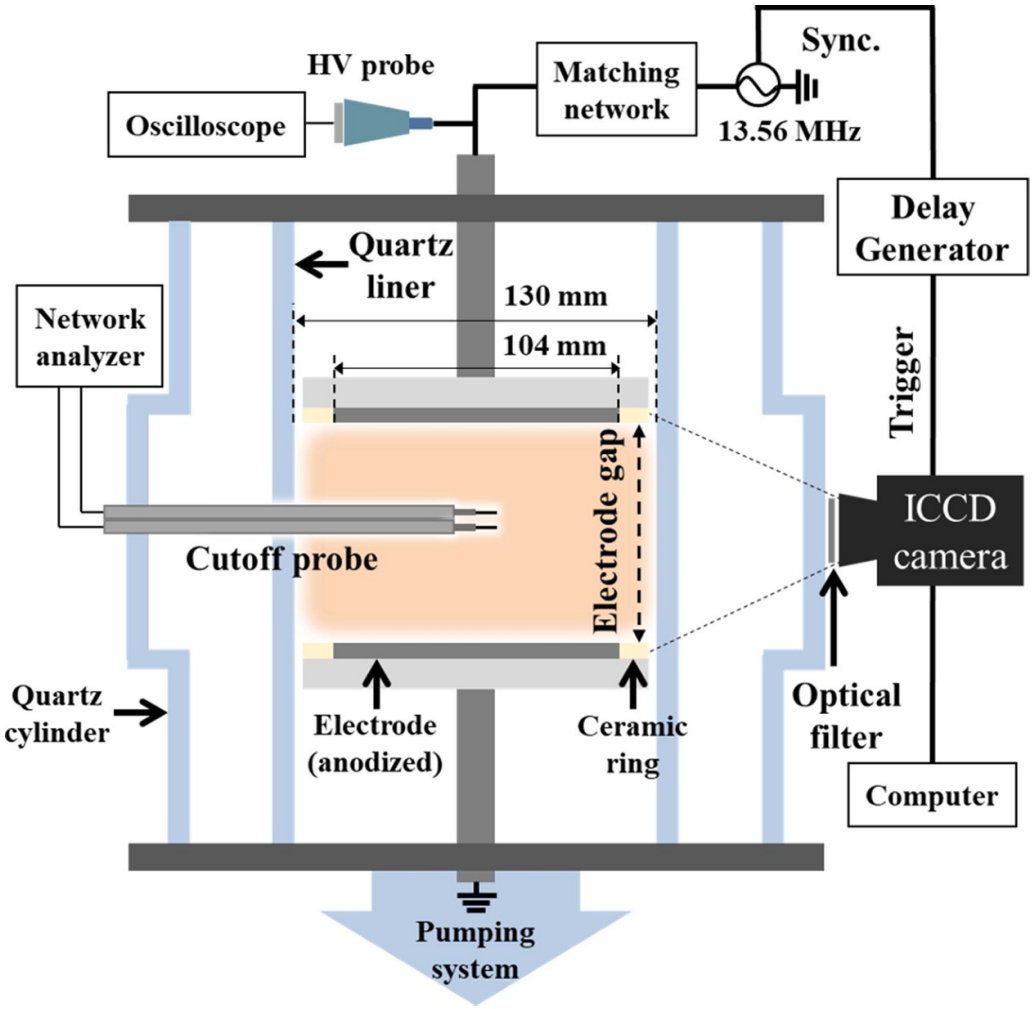

Figure 1. Schematic diagram of the experimental setup.

simulations, the plasma is generated inside a cylinder made of quartz. An additional quartz cylinder (liner) with an inner diameter of 130 mm and a height of 300 mm is used to confine the discharge in the inter-electrode space. The electrodes are made of anodised aluminium plates (Al_2O_3) with diameters of 104 mm and they are held in position by alumina rings with diameters of 127 mm. The distance between the two electrodes can be adjusted from 50 mm to 90 mm using stepper motors. RF power is applied to the top electrode at a frequency of 13.56 MHz using an RF generator (RF-5S, Advanced Energy) and a matching network, while the bottom electrode is grounded. The RF voltage waveform is monitored close to the powered electrode by a high-voltage probe (P6015A, Tektronix Inc.) connected to an oscilloscope (TDS 2000B, Tektronix Inc.). A neon gas flow of 7.5 sccm is injected into the reactor via a mass flow controller and the pressure is measured using a capacitance manometer gauge calibrated with a standard pressure gauge at the Korea Research Institute of Standards and Science.

The electron density is measured by a microwave cutoff probe [85]. This probe is inserted into the centre of the plasma and is connected to a network analyser. A stainless steel tube with a diameter of 1/4 inch is used as the probe body. The probe comprises two antennas positioned 20 mm apart, with one transmitting and the other receiving a frequency-swept signal generated by an input power of −15 dBm (0.03 mW). The transmitted signal passes through the plasma and is reflected at a certain frequency called the cutoff frequency, ω_{cutoff}, which corresponds to the electron plasma frequency, ω_{pe}. The electron density, n_{e}, can be obtained based on the following equation [86]:

$$\omega_{\mathrm{cutoff}} = \omega_{\mathrm{pe}} = \sqrt{\frac{e^2 n_{\mathrm{e}}}{\epsilon_0 m}}. \tag{1}$$

Here, m, e, and ϵ_0 are the electron mass, the elementary charge, and the permittivity of vacuum, respectively. The microwave cutoff probe directly measures the electron density by determining this cutoff frequency with an uncertainty of less than 2% without any specific assumptions [86, 87]. This accuracy holds for the plasma conditions in the presence of the probe and perturbation of the discharge by the presence of the probe itself seems to be very low due to its small size and low power input. In this study potential effects of sheaths

that form around the probe tips on the measurement accuracy can be ignored, because the sheath width is shorter than the distance between the probe tips [88, 89].

The PROES measurements are conducted using a fast-gateable intensified charge-coupled device (ICCD) camera (PI-MAX2, Princeton Instrument) in combination with an optical filter (585 nm band pass filter, full width at half maximum of 16.7 nm) that measures the plasma emission at 585.5 nm resulting from electron de-excitation from the Ne $2p_1$ level. The ICCD camera has a spatial resolution of approximately 0.5 mm and a gate time that provides a temporal resolution of 2 ns. A delay generator (DG535, Stanford Research Systems), synchronised with the RF generator, triggers the ICCD camera to acquire two-dimensional (2D) emission images of the discharge at distinct times within the RF period. These 2D images are averaged in the horizontal direction and are converted to 1D intensity distributions along the discharge axis in this way. The ICCD camera images are averaged for a given number of recordings for a given delay time between the camera trigger signal and gate. Then, the delay time is increased by the gate width and the discharge emission at the next phase within the RF period is measured. After scanning over one RF period in this way, the 1D intensity distributions taken with different delay times provide the spatio-temporal distribution of the emission at this wavelength.

Since cascade contributions to the population density and stepwise excitation of the Ne $2p_1$ level are negligible, the following equation can be used to obtain the electron-impact excitation rate from the ground state into the Ne $2p_1$ level, $E_{0,2p_1}$, space and time resolved within the RF period from the measured emission [82, 83]:

$$E_{0,2p_1} = \frac{1}{A_{2p_1,k} n_0} \left(\frac{\mathrm{d}\dot{n}_{\mathrm{ph},2p_1}(t)}{\mathrm{d}t} + A_{2p_1} \dot{n}_{\mathrm{ph},2p_1}(t) \right). \quad (2)$$

Here, n_0 is the ground state density, $A_{2p_1,k}$ is the Einstein coefficient for the observed optical transition, $\dot{n}_{\mathrm{ph},2p_1}$ is the measured number of photons per unit volume and time, and A_{2p_1} is the decay rate (the inverse of the lifetime) of the Ne $2p_1$ level. The constants $A_{2p_1,k}$ and n_0 do not have to be known to obtain the relative changes of the electron impact excitation rate, which is sufficient to get a meaningful insight into the spatio-temporal distribution of the excitation rate into the Ne $2p_1$ level. As the energy threshold for electron impact excitation from the ground state into the Ne $2p_1$ level is 19 eV, the dynamics of energetic electrons above this threshold energy is revealed by measuring $E_{0,2p_1}$ space and time resolved.

In order to obtain experimental results as a function of external control parameters, the electrode gap (50–90 mm), the neutral gas pressure (20–50 mTorr), and the peak-to-peak value of the driving voltage waveform (250–650 V) are varied systematically.

3. Simulation model

The simulations are performed by using a 1d3v PIC/MCC simulation code. The particles traced in the simulations are electrons and Ne^+ ions. The collision processes considered in the model are listed in table 1. For the collision of electrons with atoms of the background neon gas, elastic scattering (process 1), excitation (processes 2–10) and ionization (process 11) are considered. The cross sections for these processes are taken from the Biagi-v7.1 dataset [90], which includes nine atomic excitation processes. The Ne $2p_1$ electron impact excitation process from the ground state (process 10) is the one whose population dynamics is captured experimentally by the PROES measurements. For the collisions of Ne^+ ions with Ne atoms, isotropic and backward elastic scattering processes are considered (processes 12 and 13, respectively) with cross sections taken from [91]. The cross sections of the collision processes are shown in figure 2.

Table 1. List of collision processes for Neon CCPs.

#	Reaction	Process	References
1	$e^- + Ne \longrightarrow e^- + Ne$	Elastic scattering	[90]
2	$e^- + Ne \longrightarrow e^- + Ne^*$	$1s_5$ excitation	[90]
3	$e^- + Ne \longrightarrow e^- + Ne^*$	$1s_4$ excitation	[90]
4	$e^- + Ne \longrightarrow e^- + Ne^*$	$1s_3$ excitation	[90]
5	$e^- + Ne \longrightarrow e^- + Ne^*$	$1s_2$ excitation	[90]
6	$e^- + Ne \longrightarrow e^- + Ne^*$	$\sum 2p_{10-2}$ excitation	[90]
7	$e^- + Ne \longrightarrow e^- + Ne^*$	$\sum 2s$ excitation	[90]
8	$e^- + Ne \longrightarrow e^- + Ne^*$	$\sum 3d + \sum 3s$ excitation	[90]
9	$e^- + Ne \longrightarrow e^- + Ne^*$	$\sum 3p$ excitation	[90]
10	$e^- + Ne \longrightarrow e^- + Ne^*$	$2p_1$ excitation	[90]
11	$e^- + Ne \longrightarrow 2e^- + Ne^+$	Ionisation	[90]
12	$Ne^+ + Ne \longrightarrow Ne^+ + Ne$	Isotropic scattering	[91]
13	$Ne^+ + Ne \longrightarrow Ne^+ + Ne$	Backscattering	[91]

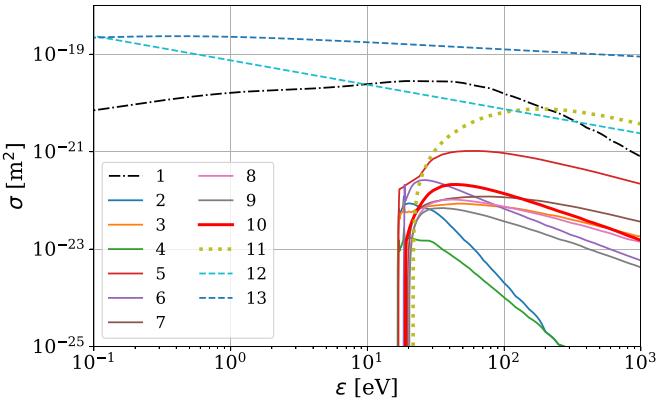

Figure 2. The cross section set used in the PIC/MCC simulations of neon CCPs, listed in table 1 (processes 1–13). ε is the kinetic energy of the projectile (ε is measured in the centre-of-mass frame in case of ions). The dash-dot line corresponds to the electron–atom elastic scattering (process 1), while the thin solid lines correspond to the electron–atom excitation channels (processes 2–10). The thick solid red line represents the Ne $2p_1$ electron-impact excitation from the ground state, which is measured by PROES (process 10). The thick dotted green line corresponds to electron-impact ionisation (process 11). The dashed lines represent ion–atom isotropic elastic scattering and elastic backscattering (processes 12 and 13), respectively.

Table 2. Parameters of the realistic model of electron–surface interaction for Al_2O_3 surfaces.

#	Parameter	Description	Value	References
1	ε_0	Threshold energy for electron-induced SEE	15 eV	[94]
2	$\varepsilon_{max,0}$	Energy of primary electrons at the maximum emission	600 eV	[95]
3	$\sigma_{max,0}$	Maximum emission at normal incidence	6	[95]
4	k_s	Smoothness factor of the surface	1	[76]
5	$\varepsilon_{e,0}$	Threshold energy for elastic reflection	0 eV	[96]
6	$\varepsilon_{e,max}$	Energy of primary electrons at the maximum elastic reflection	5 eV	[97]
7	$\eta_{e,max}$	Maximum of the elastic reflection	0.5	[97]
8	Δ_e	Control parameter for the decay of η_e	5 eV	[96]
9	r_e	Portion of elastically reflected electrons	0.03	[94]
10	r_i	Portion of inelastically reflected electrons	0.07	[94]

At the surfaces, a simplified treatment of heavy particle induced SEE is considered, by assuming a constant effective SEE probability, γ, per incident Ne^+ ion, of which the value is varied between 0 and 0.3. For electrons, two different models are used to describe their interaction with the surfaces: (i) in the first approach, only elastic electron reflection is considered, by a constant η_e coefficient. Its value is varied between $\eta_e = 0$ (electron reflection neglected) and $\eta_e = 0.2$ [92]. (ii) In the second approach, the electron–surface interaction is described according to a realistic model, presented in [70, 93]. In this approach, the surface properties are taken into account via material specific input parameters, and the emission coefficients for the elastic reflection, η_e, inelastic reflection, η_i, and electron-induced SEE, δ, are determined as functions of the energy and angle of incidence of primary electrons. Here, the parameters of the model are set for Al_2O_3 surfaces, based on experimental data from [76, 94–97] (see the details in table 2). The total electron-induced SEEC, $\sigma = \eta_e + \eta_i + \delta$, and the partial emission coefficients for Al_2O_3 surfaces as a function of the incident electron energy at normal incidence are shown in figure 3. The simulation results obtained for the different surface coefficients are compared with experimental measurements of the electron density and the spatio-temporally resolved electron impact excitation rate from the ground state into the Ne $2p_1$ level to validate the simulation and find the correct values of these surface coefficients under the conditions studied experimentally.

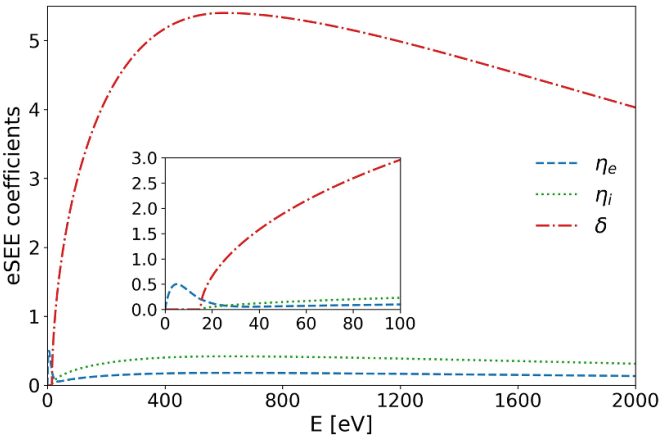

Figure 3. Energy-dependent surface coefficients for the electron–surface interactions on Al_2O_3 surfaces, for normal incidence: the total electron-induced SEEC, σ, and the partial emission coefficients of elastic electron reflection, η_e, inelastic electron backscattering, η_i, and electron-induced SEE, δ.

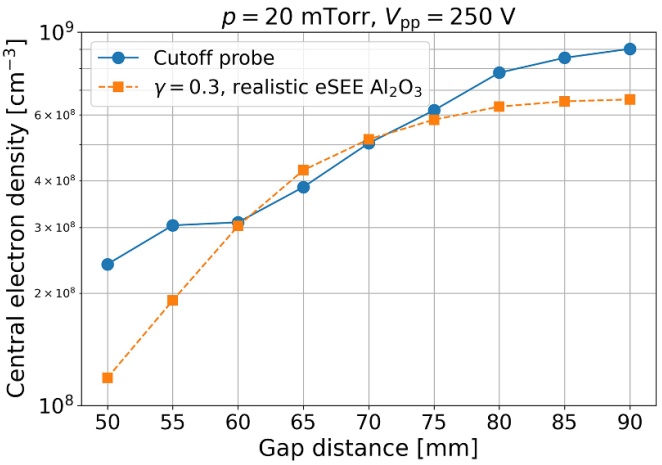

Figure 4. Electron density measured in the centre of the discharge by the cutoff probe and obtained from the PIC/MCC simulations as a function of the electrode gap at 20 mTorr and 250 V peak-to-peak voltage of the 13.56 MHz driving voltage, in the presence of Al_2O_3 electrodes. The simulation results are obtained with $\gamma = 0.3$ and the realistic electron–surface model (eSEE Al_2O_3).

4. Results

Figure 4 shows a comparison of the electron density measured by the microwave cutoff probe in the discharge centre with the corresponding electron density obtained from the PIC/MCC simulation as a function of the electrode gap, which is varied from 50 mm to 90 mm. Ne gas is used at 20 mTorr and at a peak-to-peak driving voltage of 250 V in the presence of Al_2O_3 electrodes. In the simulation, the effective heavy particle induced and electron induced SEECs were varied systematically. The best agreement between the computational and the experimental results was found for $\gamma = 0.3$ and by using the realistic electron–surface model (eSEE Al_2O_3). Only the simulation data for this choice of the surface coefficients are shown in figure 4. The effects of using different surface

coefficients on the quality of the agreement between experimental and simulation results will be discussed in more detail later. The electron density increases as a function of the electrode gap in case of both the experimental and computational results. At medium values of the gap of 60–75 mm, the computed electron density is in excellent agreement with the experimental data (with a deviation of only 3%–10%). For narrower and wider gap distances, the measured electron density is higher than the one obtained from the simulation. For the lowest gap, the measured density is higher by a factor of about 2 compared to the simulation. At the largest gap the measured density is about 30% higher. This is caused by the fact that the applicability of the 1D simulation is limited at the smallest and largest gap distances, respectively. At small electrode gaps the electron density is very low and, thus, in the experiment a large sheath is formed at the sidewalls. This effect, which cannot be captured by the 1D simulation, leads to a reduced width of the quasineutral plasma bulk in radial direction, since the reactor volume close to the confinement cylinder, i.e. the region close to the electrode edge, is covered by the large sheath adjacent to the sidewalls. Thus, the radius of the quasineutral plasma is reduced, while the electrode radius remains the same. This limits the applicability of the 1D simulation, which assumes that the radius of the quasineutral plasma is much larger than the electrode gap. In the experiment, the presence of the large sidewall sheath leads to additional electron power absorption and electron confinement by interactions of electrons with the large sidewall sheaths and to a constriction of the quasineutral plasma volume. Thus, more power is dissipated to electrons in a smaller volume in the experiment so that the electron density for small electrode gaps is higher in the experiment than in the simulations, which do not include these effects. For wide electrode gaps, the applicability of the 1D simulation might be limited again, since the electrode gap gets comparable to the electrode diameter in the experiment. This is no longer a 1D scenario. For instance, at the radial edge of the electrodes, where the quartz wall is in close vicinity to the electrode, a curved sheath can be formed. During the sheath expansion phase, energetic electron beams can be generated, which do not propagate in the direction perpendicular to the electrodes, but under a different angle [54]. In case of large electrode gaps, such energetic electron beams can propagate further towards the radial centre of the plasma, where the electron density is measured, and enhance the electron density by ionisation. This is qualitatively different from the scenario of smaller gaps, when such beams generated at the radial edge reach the opposite electrode quickly and get lost without propagating far in radial direction. All in all, surface effects can cause a higher electron density in the experiment compared to the simulation at the low and the high gap region. To verify the hypotheses above, 2D simulations would be required, which are out of the scope of the current study.

Figure 5 shows the spatio-temporal distribution of the electron impact excitation rate from the ground state into the Ne $2p_1$ level for different electrode gaps as measured by PROES and computed by the PIC/MCC simulations for the same discharge conditions as those shown in figure 4. In each panel, the vertical axis indicates the distance from the powered electrode and the horizontal axis corresponds to the time within the RF period. The left column shows the experimental results, while the right column corresponds to the simulation. The gap between the electrodes increases row by row. In the PIC/MCC simulation results, the sheath edges are shown as red lines (calculated as proposed in [98]), while the sheaths can be identified as blue regions of low excitation rate in the PROES results. As the electrode gap distance increases, a gradual decrease of the maximum sheath width is found in both the experimental and the computed distributions, since the electron density increases as a function of the electrode gap at fixed peak-to-peak driving voltage. For each electrode gap, the maximum sheath width is approximately the same based

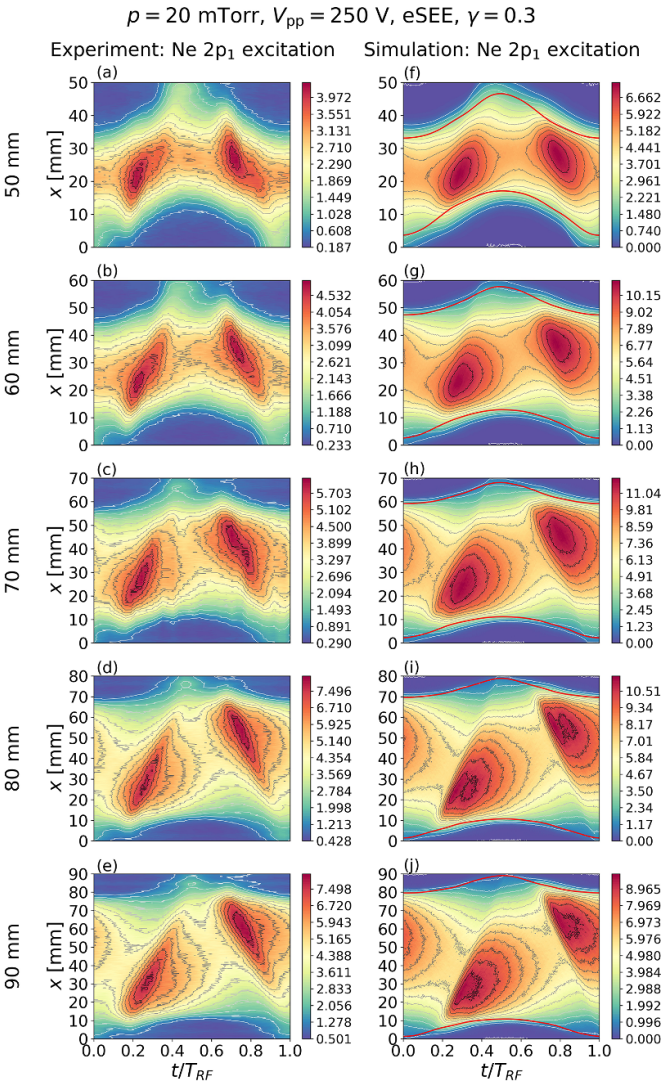

Figure 5. Spatio-temporal plots of the electron impact excitation rate from the ground state into the Ne $2p_1$ level measured by PROES, for different electrode gaps ((a)–(e) in a.u.) and computed by the PIC/MCC simulations ((f)–(j) in units of $10^{18}\,\mathrm{m^{-3}\,s^{-1}}$). Discharge conditions: $f = 13.56$ MHz, $V_{pp} = 250$ V, $p = 20$ mTorr. The red lines in the right column indicate the position of the sheath edge calculated according to [98].

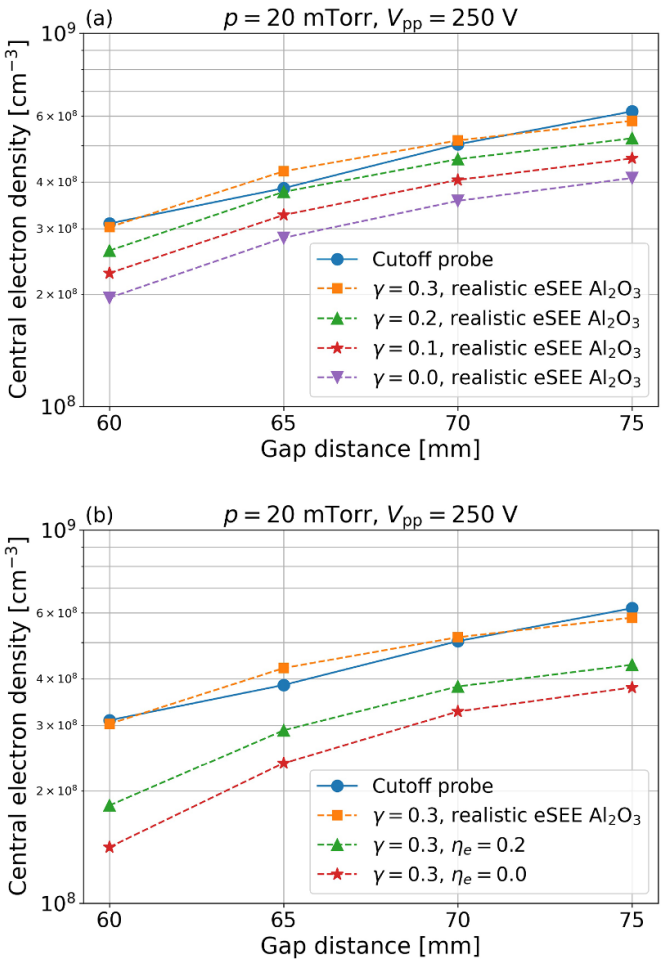

Figure 6. Electron density in the centre of the discharge obtained by microwave cutoff probe measurements and PIC/MCC simulations assuming (a) various γ-coefficients while using the realistic electron–surface model and (b) different η_e-coefficients with $\gamma = 0.3$, as a function of the electrode gap length. Discharge conditions: neon gas, Al_2O_3 electrodes, $f = 13.56$ MHz, $V_{pp} = 250$ V, $p = 20$ mTorr.

on the experiment and the simulation, in accordance with the good quantitative agreement of the plasma densities (see figure 4). A general feature of these spatio-temporal plots of the excitation rate is that energetic electron beams are generated near the sheath edges during their expansion phase and penetrate into the bulk plasma contributing to the excitation dynamics, as shown both by PROES and by PIC/MCC simulations. This is due to ambipolar/pressure heating of electrons during the sheath expansion phase [43, 99]. The plasma is operated in the α-mode under the conditions studied here. Overall, the spatio-temporal distributions of the excitation rate obtained by the PIC/MCC simulations are in good agreement with the PROES measurements for all electrode gaps studied. In combination with the good agreement of the electron density, this corresponds to a successful multi-diagnostic experimental validation of the simulation for Ne gas at low pressure.

The effects of changing the heavy particle induced SEEC, γ, and the electron–surface interaction model in the simulation are illustrated by figure 6, which shows the electron density as a function of the electrode gap between 60 mm and 75 mm. As discussed before, the 1D simulation is most applicable in this range of electrode gaps and the best agreement between experimental and computational results is found for $\gamma = 0.3$ in combination with the realistic electron–surface interaction model for Al_2O_3. Decreasing γ leads to a decrease of the electron density obtained from the simulations (see figure 6(a)) due to a lower contribution of heavy particle induced SEs to the ionization and to the emission of δ-electrons. Correspondingly, a lower γ causes worse agreement between the experimental and the simulation results. In figure 6(b), the effect of keeping $\gamma = 0.3$ unchanged and replacing the realistic electron–surface interaction model in the simulation by a constant elastic electron reflection probability of $\eta_e = 0$ or $\eta_e = 0.2$ and neglecting inelastic electron reflection and electron-induced SEE is shown. Applying $\eta_e = 0.2$ results in lower plasma densities and worse agreement between the experiment and the simulation (see figure 6(b)). This happens mainly because electron-induced SEs are not included in this model and they cannot contribute to the number of electrons and the ionization dynamics. Moreover, the quality of electron confinement is reduced further by completely neglecting electron reflection by setting $\eta_e = 0$, resulting in even lower plasma densities and worse agreement with the experiment.

Figure 7(a) shows the electron density obtained from the experiment and the simulation as a function of the peak-to-peak driving voltage at a fixed neutral gas pressure of 20 mTorr and electrode gap of 50 mm. In the simulation, the surface coefficients for which the best agreement between the experiment and the simulation was found in case of the electrode gap variation are used, i.e. $\gamma = 0.3$ and the realistic electron-surface interaction model. A good agreement between the experimental and the computational results is found for the same set of surface coefficients: the densities obtained from the experiment and the simulation are practically equal at the highest voltage of 650 V, and the difference is below a factor of two at lower voltages. In figure 7(b), the electron density is shown for a fixed electrode gap distance of 50 mm and a fixed peak-to-peak driving voltage of 650 V, as a function of the neutral gas pressure, obtained experimentally and computationally. Similarly to the series above, reasonable qualitative agreement is found between the trends, and the densities are practically equal at the lowest pressure of 20 mTorr, while the difference is within a factor of 2 at higher pressures as well. The deviations of the simulation results from the measured density observed in figures 7(a) and (b) at some points can be caused by the fact that in reality, the heavy particle induced SEEC changes as a function of the pressure and the voltage, since these discharge conditions influence the energy distribution of ions bombarding the electrodes, and SEE typically depends on the particle energies. This could be investigated by including realistic SEEC for the ions in the PIC/MCC simulation, yet it remains beyond the scope of the current paper.

Overall and within the range of electrode gaps, neutral gas pressure, and peak-to-peak driving voltages studied in this

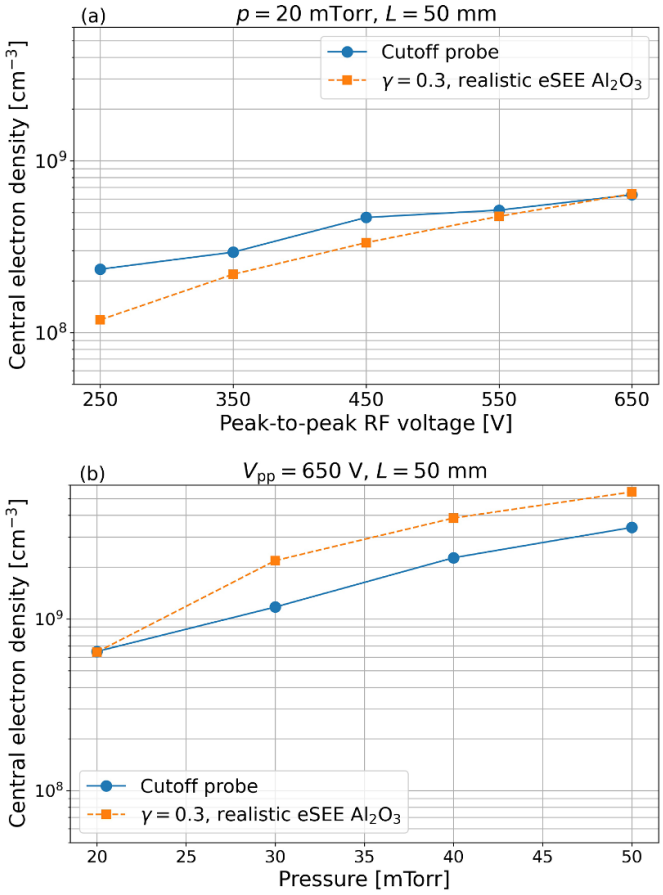

Figure 7. Electron density in the centre of the discharge obtained by microwave cutoff probe measurements and PIC/MCC simulations as a function of (a) peak-to-peak RF voltage for a fixed electrode gap of 50 mm and pressure of 20 mTorr and (b) pressure at a fixed electrode gap of 50 mm and peak-to-peak driving voltage of 650 V. $\gamma = 0.3$ and realistic electron–surface model are used in the PIC/MCC simulation. Discharge conditions: 13.56 MHz, neon gas, Al_2O_3 electrodes.

work, the experimental results can be described in a quantitatively correct way by the simulation based on the choice of a heavy particle induced effective SEEC of $\gamma = 0.3$ in combination with a realistic electron–surface interaction model for Al_2O_3 surfaces. This result indicates that these surface coefficients are correct for the electrode surface material and within the range of external control parameters used in this work. The results obtained validate the PIC/MCC simulation in neon gas under different conditions at low pressure, and they provide a good basis for future simulation based plasma process development in CCPs. However, we note that the SEECs depend on the surface materials as well as the energy and angle of incident particles. Therefore, such quantitative experimental validation studies of simulations should be extended to other surface materials and to a broader range of plasma conditions including very high driving voltages, which would lead to higher ion bombardment energies and, thus, potentially to different values of γ at the electrodes. Moreover, experimental validation studies should be performed for 2D simulations and for more complex reactive gas mixtures to develop quantitatively accurate simulation tools that can be used for knowledge based plasma process development under application relevant discharge conditions.

5. Conclusions

1d3v PIC/MCC simulations of low pressure capacitively coupled RF plasmas operated in neon at 13.56 MHz with electrodes made of Al_2O_3 were validated against experiments as a function of the electrode gap, neutral gas pressure and peak-to-peak value of the driving voltage waveform. In the frame of the experiments, the central electron density and the spatio-temporally resolved electron impact excitation rate from the ground state into the Ne $2p_1$ level were measured by a microwave cutoff probe and PROES, respectively.

The quality of the agreement between computational and experimental results for the electron density was found to depend on the choice of the surface coefficients for heavy particle induced SEE, γ, and electron–surface interactions. For the latter, a material specific and realistic model was found to provide the best agreement with the experimental results. In this model, elastic and inelastic electron reflection as well as electron-induced SEE were taken into account by coefficients depending on the energy and the angle of incidence of the bombarding electrons. Regarding the interaction of heavy particles with the electrodes, an effective ion-induced SEE coefficient of $\gamma = 0.3$ was found to yield good agreement with experimental results for all variations of the external control parameters performed in this work. Using a simplified electron–surface interaction model, where only constant elastic electron reflection probabilities of 0 or 0.2 were used, was found to yield remarkably lower densities compared to the experimental data.

For short electrode gaps, at which the electron density is low and the sheaths at the sidewalls are wide, and for very large gaps, at which the electrode gap becomes comparable to the electrode diameter in the experiment, limitations of the applicability of the 1D simulations were found to reduce the quality of the agreement of the simulation with the experimental results.

Regarding the spatio-temporal distributions of the excitation rate of the Ne $2p_1$ level, the PIC/MCC simulations provided good qualitative agreement with the PROES measurements, and the estimated width of the sheaths also matched.

Overall, within the range of electrode gaps at which the 1D simulation approach is applicable, good agreement between simulation and experimental results was found. This successful multi-diagnostic experimental validation of the 1d3v PIC/MCC simulation provides the basis of reliable plasma process development based on computational predictions. Clearly, such validation studies should be extended in the

future to more complex reactive gases and gas mixtures relevant for plasma processing applications.

Data availability statement

The data that support the findings of this study are available upon reasonable request from the authors.

Acknowledgments

This work was supported by the Hungarian National Research, Development and Innovation Office via Grants K-134462 and FK-128924, by the ÚNKP-22-3 New National Excellence Program of the Ministry for Culture and Innovation of Hungary from the source of the National Research, Development and Innovation Fund, by the German Research Foundation (DFG) within the frame of the collaborative research centre SFB 1316 (project A4), the Material Innovation Program (Grant No. 2020M3H4A3106004) of the National Research Foundation of Korea funded by Ministry of Science and ICT, the R & D Convergence Program (CRC-20-01-NFRI) of the National Research Council of Science & Technology of Republic of Korea, the Industrial Fundamental Technology Development Program of the Ministry of Trade, Industry & Energy (1415187722) and the Korea Semiconductor Research Consortium (RS-2023-00235950).

ORCID iDs

Chan-Won Park https://orcid.org/0009-0008-3723-6611
B Horváth https://orcid.org/0000-0002-2371-2444
A Derzsi https://orcid.org/0000-0002-8005-5348
J Schulze https://orcid.org/0000-0001-7929-5734
J H Kim https://orcid.org/0000-0002-7197-6073
Z Donkó https://orcid.org/0000-0003-1369-6150
Hyo-Chang Lee https://orcid.org/0000-0003-2754-1512

References

[1] Lieberman M A and Lichtenberg A J 2005 *Principles of Plasma Discharges and Materials Processing* 2nd edn (Wiley)
[2] Chabert P and Braithwaite N 2011 *Physics of Radio-Frequency Plasmas* (Cambridge University Press)
[3] Makabe T and Petrović Z 2006 *Plasma Electronics: Applications in Microelectronic Device Fabrication* (Taylor and Francis)
[4] Donnelly V M and Kornblit A 2013 *J. Vac. Sci. Technol.* **31** 050825
[5] Lee H-C 2018 *Appl. Phys. Rev.* **5** 011108
[6] Vahedi V, Birdsall C K, Lieberman M A, DiPeso G and Ronhlien T D 1993 *Plasma Sources Sci. Technol.* **2** 273
[7] Donkó Z 2001 *Phys. Rev.* E **64** 026401
[8] Turner M M 2006 *Phys. Plasmas* **13** 033506
[9] Wilczek S *et al* 2016 *Phys. Plasmas* **23** 063514
[10] Gudmundsson J T, Kawamura E and Lieberman M A 2013 *Plasma Sources Sci. Technol.* **22** 035011
[11] Daksha M, Derzsi A, Wilczek S, Trieschmann J, Mussenbrock T, Awakowicz P, Donkó Z and Schulze J 2017 *Plasma Sources Sci. Technol.* **26** 085006
[12] Horváth B, Derzsi A, Schulze J, Korolov I, Hartmann P and Donkó Z 2020 *Plasma Sources Sci. Technol.* **29** 055002
[13] Denpoh K 2020 *Jpn. J. Appl. Phys.* **60** 016002
[14] Denpoh K and Nanbu K 2022 *J. Vac. Sci. Technol.* **40** 063007
[15] Sun A, Becker M M and Loffhagen D 2018 *Plasma Sources Sci. Technol.* **27** 054002
[16] Gudmundsson J T, Krek J, Wen D-Q, Kawamura E and Lieberman M A 2022 *Plasma Sources Sci. Technol.* **30** 125011
[17] Yang D, Wang H, Zheng B, Zou X, Wang X and Fu Y 2022 *Plasma Sources Sci. Technol.* **31** 115002
[18] Donkó Z 2011 *Plasma Sources Sci. Technol.* **20** 024001
[19] Wen D-Q, Krek J, Gudmundsson J T, Kawamura E, Lieberman M A and Verboncoeur J P 2022 *IEEE Trans. Plasma Sci.* **50** 2548–57
[20] Kushner M J 2009 *J. Phys. D: Appl. Phys.* **42** 194013
[21] Zhang Y-R, Huang J-W, Zhou F-J, Lu C, Sun J-Y, Su Z-X and Wang Y-N 2023 *Plasma Sources Sci. Technol.* **32** 054005
[22] Georgieva V, Bogaerts A and Gijbels R 2004 *Phys. Rev.* E **69** 026406
[23] Schulze J, Donkó Z, Luggenhölscher D and Czarnetzki U 2009 *Plasma Sources Sci. Technol.* **18** 034011
[24] Schulze J, Donkó Z, Schüngel E and Czarnetzki U 2011 *Plasma Sources Sci. Technol.* **20** 045007
[25] Heil B G, Czarnetzki U, Brinkmann R P and Mussenbrock T 2008 *J. Phys. D: Appl. Phys.* **41** 165202
[26] Donkó Z, Schulze J, Heil B G and Czarnetzki U 2008 *J. Phys. D: Appl. Phys.* **42** 025205
[27] Korolov I, Donkó Z, Czarnetzki U and Schulze J 2012 *J. Phys. D: Appl. Phys.* **45** 465205
[28] Lafleur T 2016 *Plasma Sources Sci. Technol.* **25** 013001
[29] Buzzi F L, Ting Y-H and Wendt A E 2009 *Plasma Sources Sci. Technol.* **18** 025009
[30] Agarwal A and Kushner M J 2005 *J. Vac. Sci. Technol.* A **23** 1440–9
[31] Hartmann P, Korolov I, Escandon-Lopez J, van Gennip W, Buskes K and Schulze J 2022 *Plasma Sources Sci. Technol.* **31** 055017
[32] Hartmann P, Korolov I, Escandon-Lopez J, van Gennip W, Buskes K and Schulze J 2023 *J. Phys. D: Appl. Phys.* **56** 055202
[33] Sommerer T J and Kushner M J 1992 *J. Appl. Phys.* **71** 1654–73
[34] Huang S, Huard C, Shim S, Nam S K, Song I-C, Lu S and Kushner M J 2019 *J. Vac. Sci. Technol.* A **37** 031304
[35] Niemi K, von der Gathen V S and Döbele H F 2001 *J. Phys. D: Appl. Phys.* **34** 2330
[36] Preissing P, Korolov I, Schulze J, Schulz-von der Gathen V and Böke M 2020 *Plasma Sources Sci. Technol.* **29** 125001
[37] Steuer D, Korolov I, Chur S, Schulze J, Schulz-von der Gathen V, Golda J and Böke M 2021 *J. Phys. D: Appl. Phys.* **54** 355204
[38] Babkina T, Gans T and Czarnetzki U 2005 *Europhys. Lett.* **72** 235–41
[39] Ellerweg D, Benedikt J, von Keudell A, Knake N and Schulz-von der Gathen V 2010 *New J. Phys.* **12** 013021
[40] Belenguer P and Boeuf J P 1990 *Phys. Rev.* A **41** 4447–59
[41] Schulze J, Heil B G, Luggenholscher D and Czarnetzki U 2008 *IEEE Trans. Plasma Sci.* **36** 1400–1
[42] Turner M M 2009 *J. Phys. D: Appl. Phys.* **42** 194008
[43] Schulze J, Donko Z, Lafleur T, Wilczek S and Brinkmann R P 2018 *Plasma Sources Sci. Technol.* **27** 055010
[44] Daksha M, Derzsi A, Mujahid Z, Schulenberg D, Berger B, Donkó Z and Schulze J 2019 *Plasma Sources Sci. Technol.* **28** 034002

[45] Schulze J, Derzsi A, Dittmann K, Hemke T, Meichsner J and Donkó Z 2011 *Phys. Rev. Lett.* **107** 275001
[46] Bischoff L *et al* 2018 *Plasma Sources Sci. Technol.* **27** 125009
[47] Proto A and Gudmundsson J T 2020 *J. Appl. Phys.* **128** 113302
[48] Proto A and Gudmundsson J T 2021 *Plasma Sources Sci. Technol.* **30** 065009
[49] Liu Y-X, Schüngel E, Korolov I, Donkó Z, Wang Y-N and Schulze J 2016 *Phys. Rev. Lett.* **116** 255002
[50] Liu Y-X, Korolov I, Schüngel E, Wang Y-N, Donko Z and Schulze J 2017 *Plasma Sources Sci. Technol.* **26** 055024
[51] Wang M and Kushner M J 2010 *J. Appl. Phys.* **107** 023308
[52] Kruger F, Lee H, Nam S K and Kushner M J 2021 *Plasma Sources Sci. Technol.* **30** 085002
[53] Krüger F, Lee H, Nam S K and Kushner M J 2023 *J. Vac. Sci. Technol.* A **41** 013006
[54] Wang L, Hartmann P, Donko Z, Song Y-H and Schulze J 2021 *J. Vac. Sci. Technol.* A **39** 063004
[55] Park H, Sakiyama Y and Lee H J 2023 *Front. Phys.* **11** 1137994
[56] Yang Y and Kushner M J 2010 *J. Phys. D: Appl. Phys.* **43** 152001
[57] Chen Z, Kenney J, Rauf S, Collins K, Tanaka T, Hammond N and Kudela J 2011 *IEEE Trans. Plasma Sci.* **39** 2526–7
[58] Schmidt N, Schulze J, Schüngel E and Czarnetzki U 2013 *J. Phys. D: Appl. Phys.* **46** 505202
[59] Ohtsu Y, Matsumoto N, Schulze J and Schuengel E 2016 *Phys. Plasmas* **23** 033510
[60] Wen D-Q, Krek J, Gudmundsson J T, Kawamura E, Lieberman M A and Verboncoeur J P 2021 *Plasma Sources Sci. Technol.* **30** 105009
[61] Turner M M, Derzsi A, Donko Z, Eremin D, Kelly S J, Lafleur T and Mussenbrock T 2013 *Phys. Plasmas* **20** 013507
[62] Schulenberg D A, Korolov I, Donko Z, Derzsi A and Schulze J 2021 *Plasma Sources Sci. Technol.* **30** 105003
[63] Schulze C, Donkó Z and Benedikt J 2022 *Plasma Sources Sci. Technol.* **31** 105017
[64] Daksha M, Berger B, Schüengel E, Korolov I, Derzsi A, Koepke M, Donkó Z and Schulze J 2016 *J. Phys. D: Appl. Phys.* **49** 234001
[65] Derzsi A, Hartmann P, Vass M, Horváth B, Gyulai M, Korolov I, Schulze J and Donkó Z 2022 *Plasma Sources Sci. Technol.* **31** 085009
[66] Raitses Y, Kaganovich I D, Khrabrov A, Sydorenko D, Fisch N J and Smolyakov A 2011 *IEEE Trans. Plasma Sci.* **39** 995–1006
[67] Lafleur T, Chabert P and Booth J P 2013 *J. Phys. D: Appl. Phys.* **46** 135201
[68] Greb A, Niemi K, O'Connell D and Gans T 2013 *Appl. Phys. Lett.* **103** 244101
[69] Liu Q, Liu Y, Samir T and Ma Z 2014 *Phys. Plasmas* **21** 083511
[70] Horváth B, Daksha M, Korolov I, Derzsi A and Schulze J 2017 *Plasma Sources Sci. Technol.* **26** 124001
[71] Horváth B, Schulze J, Donkó Z and Derzsi A 2018 *J. Phys. D: Appl. Phys.* **51** 355204
[72] Sun J-Y, Wen D-Q, Zhang Q-Z, Liu Y-X and Wang Y-N 2019 *Phys. Plasmas* **26** 063505
[73] Wen D-Q, Krek J, Gudmundsson J T, Kawamura E, Lieberman M A, Zhang P and Verboncoeur J P 2023 *Plasma Sources Sci. Technol.* **32** 064001
[74] Derzsi A, Korolov I, Schüngel E, Donkó Z and Schulze J 2015 *Plasma Sources Sci. Technol.* **24** 034002
[75] Phelps A V and Petrovic Z L 1999 *Plasma Sources Sci. Technol.* **8** R21
[76] Vaughan J 1989 *IEEE Trans. Electron Devices* **36** 196–7
[77] Hagstrum H D 1954 *Phys. Rev.* **96** 336–65
[78] Buschhaus R, Prenzel M and von Keudell A 2022 *Plasma Sources Sci. Technol.* **31** 025017
[79] Wang L, Hartmann P, Donkó Z, Song Y-H and Schulze J 2021 *Plasma Sources Sci. Technol.* **30** 085011
[80] Wang L, Hartmann P, Donkó Z, Song Y-H and Schulze J 2021 *Plasma Sources Sci. Technol.* **30** 054001
[81] Horváth B, Donkó Z, Schulze J and Derzsi A 2022 *Plasma Sources Sci. Technol.* **31** 045025
[82] Schulze J, Gans T, O'Connell D, Czarnetzki U, Ellingboe A R and Turner M M 2007 *J. Phys. D: Appl. Phys.* **40** 7008
[83] Schulze J, Schüngel E, Donkó Z, Luggenhölscher D and Czarnetzki U 2010 *J. Phys. D: Appl. Phys.* **43** 124016
[84] Gans T, O'Connell D, von der Gathen V S and Waskoenig J 2010 *Plasma Sources Sci. Technol.* **19** 034010
[85] Kim J-H, Seong D-J, Lim J-Y and Chung K-H 2003 *Appl. Phys. Lett.* **83** 4725–7
[86] Kim J-H, Chung K-H and Shin Y-H 2005 *Metrologia* **42** 110
[87] Yeom H, Kim J, Choi D, Choi E, Yoon M, Seong D, You S J and Lee H-C 2020 *Plasma Sources Sci. Technol.* **29** 035016
[88] Kim D, You S, Kim J, Chang H Y and Oh W Y 2012 *Appl. Phys. Lett.* **100** 244107
[89] Yeom H, Kim Y G, Chae G S, Hwang D Y, Kim J H and Lee H C 2023 *J. Appl. Phys.* **133** 183302
[90] Biagi S F 2004 Biagi-v7.1 database cross sections extracted from PROGRAM MAGBOLTZ VERSION 7.1 JUNE 2004 (available at: www.lxcat.net) (Accessed 8 April 2019)
[91] Phelps A V 2000 personal communication
[92] Kollath R 1956 *Encyclopedia of Physics* vol 21, ed S Flügge (Springer) p 264
[93] Sydorenko D 2006 Particle-in-cell simulations of electron dynamics in low pressure discharges with magnetic fields *PhD Thesis* University of Saskatchewan, Saskatoon, Canada
[94] Gopinath V P, Verboncoeur J P and Birdsall C K 1998 *Phys. Plasmas* **5** 1535–40
[95] Insepov Z, Ivanov V and Frisch H 2010 *Nucl. Instrum. Methods Phys. Res.* B **268** 3315–20
[96] Bronshtein I M and Fraiman B S 1969 *Secondary Electron Emission* (Atomizdat)
[97] Barral S, Makowski K, Peradzyński Z, Gascon N and Dudeck M 2003 *Phys. Plasmas* **10** 4137–52
[98] Brinkmann R P 2007 *J. Appl. Phys.* **102** 093303
[99] Turner M M 1995 *Phys. Rev. Lett.* **75** 1312–5